



A photosensitizer–polyoxometalate dyad that enables the decoupling of light and dark reactions for delayed on-demand solar hydrogen production

Sebastian Amthor¹, Sebastian Knoll¹, Magdalena Heiland¹, Linda Zedler², Chunyu Li³, Djawed Nauroozi¹, Willi Tobiaschus^{4,5,6}, Alexander K. Mengele¹, Montaha Anjass^{1,7}, Ulrich S. Schubert^{4,5,6}, Benjamin Dietzek-Ivanšić^{1,2,3,6}✉, Sven Rau¹✉ and Carsten Streb^{1,7}✉

Decoupling the production of solar hydrogen from the diurnal cycle is a key challenge in solar energy conversion, the success of which could lead to sustainable energy schemes capable of delivering H₂ independent of the time of day. Here, we report a fully integrated photochemical molecular dyad composed of a ruthenium-complex photosensitizer covalently linked to a Dawson polyoxometalate that acts as an electron-storage site and hydrogen-evolving catalyst. Visible-light irradiation of the system in solution leads to charge separation and electron storage on the polyoxometalate, effectively resulting in a liquid fuel. In contrast to related, earlier dyads, this system enables the harvesting, storage and delayed release of solar energy. On-demand hydrogen release is possible by adding a proton donor to the dyad solution. The system is a minimal molecular model for artificial photosynthesis and enables the spatial and temporal separation of light absorption, fuel storage and hydrogen release.

The conversion of solar energy into storable secondary energy carriers such as hydrogen is a central concept for sustainable energy technologies^{1–3}. Due to the unpredictability of solar irradiation intensity and a mismatch between diurnal cycles and energy demand, decoupling solar energy harvesting from hydrogen evolution is a key target for advanced ‘solar hydrogen’ production^{4–6}. Also, this approach would allow the ‘on-demand’ production of hydrogen so that current challenges in hydrogen storage could be mitigated⁷. While in principle, this concept can be based on the coupling of photovoltaic cells, batteries and water electrolyzers^{8–10}, energy losses at each step add up and often result in low overall energy conversion and hydrogen generation efficiencies^{11–13}.

Pioneering studies have proposed heterogeneous multi-component (photo-)electrochemical schemes as viable alternatives to multistep photovoltaic solar hydrogen production¹⁴: in one seminal example, Symes, Cronin and colleagues used a water-oxidizing (photo-)anode to store electrons and protons on redox-active molecular metal oxides (polyoxometalates, or POMs)^{5,6,15}. Subsequent reaction of the reduced POM with a hydrogen evolution catalyst (for example, Pt metal) enabled on-demand hydrogen release. In ground-breaking studies, Reisner, Jeschke, Lotsch and colleagues demonstrated that the semiconductor carbon nitride can be used as the light absorber and electron storage site. Upon addition of a cocatalyst, for example Pt, the system was capable of delayed H₂ release in the dark¹⁶.

An alternative approach is the design of homogeneous, fully molecular systems for decoupling light and dark reactions. These systems offer ultimate control over molecular structure and thus enable the fine-tuning of light absorption, charge separation and the hydrogen evolution reaction. Pioneering studies by MacDonnell

and colleagues highlighted that multiple charges can be stored in one molecule when proton-coupled electron storage is employed to minimize structural and electrostatic changes¹⁷. Building on these seminal studies, very recently, Schulz and colleagues demonstrated that Cu(I) complexes can combine light absorption and electron storage, paving the way for noble-metal-free molecular devices for charge storage and release¹⁸.

Recently, organo-functionalized POMs, have attracted widespread attention as possible minimal models for fully integrated molecular photochemical molecular devices^{19,20}. Pioneering research demonstrated that the covalent functionalization of Keggin^{21–23}, Dawson^{22,24} or Anderson-type^{25–29} POMs with molecular photosensitizers such as metal complexes^{21,22,24–30} or organic dyes^{23,31–33} is possible. In seminal studies, Izzet, Proust, Artero and coworkers reported light-induced charge accumulation and light-driven hydrogen evolution using Ir-complex-functionalized Dawson polyoxotungstates^{22,24}. The authors demonstrated that up to two electrons could be transferred to the cluster while maintaining the structural integrity of the molecular assembly. Building on these studies, Rau and Streb have explored the linkage of metal complex PS to various POMs and observed that robust, selective and mild functionalization strategies are critical to prevent uncontrolled aggregation³⁴ or even POM and/or photosensitizer degradation^{35,36}.

Here, we build on these concepts and report the development and use of a covalent photosensitizer–polyoxometalate (PS-POM) dyad for visible-light absorption, charge separation, charge storage and hydrogen release. Crucially, the reduced PS-POM dyad can be stored and used as a liquid fuel where on-demand hydrogen evolution is possible by simple reaction of the reduced PS-POM solution

¹Institute of Inorganic Chemistry I, Ulm University, Ulm, Germany. ²Department Functional Interfaces, Leibniz Institute of Photonic Technology Jena (Leibniz IPHT), Jena, Germany. ³Institute of Physical Chemistry, Friedrich Schiller University Jena, Jena, Germany. ⁴Laboratory of Organic and Macromolecular Chemistry (IOMC), Friedrich Schiller University Jena, Jena, Germany. ⁵Jena Center of Soft Matter (JCSM), Friedrich Schiller University Jena, Jena, Germany. ⁶Center for Energy and Environmental Chemistry Jena (CEEC Jena), Friedrich Schiller University Jena, Jena, Germany. ⁷Helmholtz-Institute Ulm (HIU), Ulm, Germany. ✉e-mail: benjamin.dietzek@leibniz-ipht.de; sven.rau@uni-ulm.de; carsten.streb@uni-ulm.de

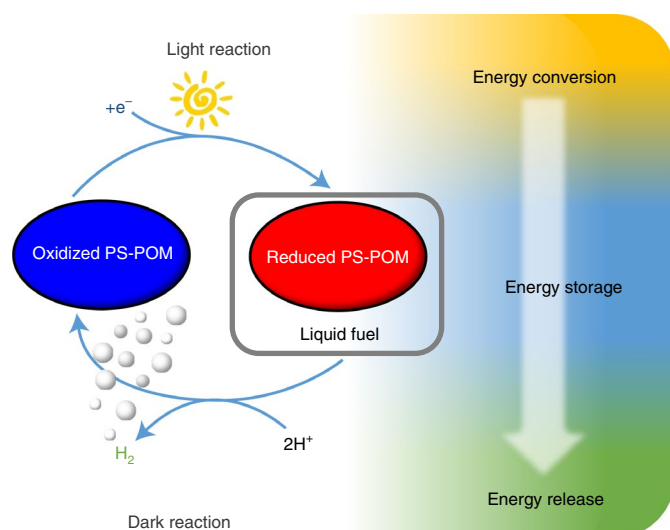


Fig. 1 | Schematic illustration of the coupled light and dark reaction. In the light reaction, a covalent PS-POM dyad is chemically reduced under irradiation (electron storage step). In the dark reaction, the reduced PS-POM dyad can be reacted with protons in solution, leading to the light-independent, delayed release of solar hydrogen. This scheme enables the temporal and spatial decoupling of light harvesting, charge separation, charge storage and hydrogen release. e^- , electron.

with a proton source, leading to the ‘dark’ release of H_2 (Fig. 1)^{22,24}. The system combines high stability under irradiation with promising hydrogen evolution yields, while the modular design based on molecular subunits will allow the independent chemical tuning and optimization of the whole system.

Results and discussion

PS-POM synthesis and characterization. The PS-POM dyad was formed by reaction of the phosphonate-functionalized Ru PS **1a** with the lacunary Dawson POM **2** ($(\alpha_2-P_2W_{17}O_{61})^{10-}$) in dichloromethane at room temperature (Fig. 2a; Supplementary Information for experimental and analytical details). **1a** was accessed by reaction of precursor **1** ($((tbbpy)_2Ru(mPO_3Et_2)bpy)$ (PF_6)₂; tbbpy, 4,4′-di-*tert*-butyl 2,2′-bipyridine; $(mPO_3Et_2)bpy$, diethyl((4′-methyl-(2,2′-bipyridin)-4-yl)methyl)phosphonate) with trimethylsilyl bromide prior to the POM functionalization, thus enabling mild reaction conditions³⁷. The traditional approach, that is, reaction of **2** with the respective phosphonic acid or phosphonic acid esters, did not lead to product formation, presumably due to cluster degradation or adduct formation by the harsh reaction conditions. Sample purity and covalent attachment of two PS units per POM were verified by 1H and ^{31}P NMR spectroscopy (Fig. 2e), matrix-assisted laser desorption ionisation (MALDI) mass spectrometry and attenuated total reflection (ATR)–infrared spectroscopy (Supplementary Section 2). Ultraviolet–visible (UV–vis) spectroscopy of PS-POM reveals the presence of a broad Ru–PS-based 1MLCT (singlet metal-to-ligand charge-transfer) transition centred at ~ 450 nm and POM-based ligand-to-metal charge-transfer (LMCT) transitions at wavelengths $\lambda < 350$ nm. These LMCT transition overlap with the ligand-centred (LC) transitions based on the 2,2′-bipyridyl (bpy) ligands of the ruthenium chromophore (Fig. 2b). Specific excitation of the Ru-based $MLCT$ charge-separating transition by irradiation with visible light ($\lambda > 400$ nm) is, therefore, possible without triggering any undesired POM-based photochemistry in the UV region³⁸.

Emission spectroscopy was used to probe the electronic interactions between PS and POM (Fig. 2c). For PS-POM, an emission

quenching of 97% compared with the pure PS was observed. By contrast, the intermolecular reference system, that is, a mixture of the precursors **1** and **2** (2:1 molar ratio), gave an emission quenching of only 45%. This can indicate strong electronic coupling in the covalent PS-POM dyad. The loss of emission quantum yield is in line with the reduced emission lifetime of PS-POM compared with the non-linked PS reference **1** (Fig. 2d). The emission lifetimes for **1** and PS-POM were measured with sub-two-nanosecond time resolution using time-correlated single-photon counting. For PS-POM, this gave a biexponential decay with lifetimes of < 2 ns (limited by instrumental response) and 62 ns. Both lifetimes are substantially lower than the fluorescence lifetime of **1** (200 ns; Supplementary Fig. 21). As discussed in detail below, these observations are a first indication of the coexistence of two PS-POM conformers with different electronic coupling.

Reversible light-induced electron storage by PS-POM. Next, we assessed the accessible redox processes of PS-POM using cyclic voltammetry in water-free, de-aerated *N,N*-dimethyl formamide (DMF) containing 0.1 M nBu_4NPF_6 as electrolyte. Cyclic voltammetry analysis shows that the one- and two-electron reduced species are accessible at redox potentials of -0.68 V (one-electron reduced) and -1.10 V (two-electron reduced) versus ferrocenium/ferrocene (Fc^+/Fc), respectively. Both processes are assigned to $W^{VI/V}$ redox couples²⁴. Electrolysis further shows that in the bulk, near-complete and reversible two-electron reduction of PS-POM is possible (reduction, 2.0 electrons per PS-POM; reoxidation, 1.8 electrons per PS-POM; Supplementary Fig. 18). In the presence of a strong acid (trifluoroacetic acid, TFA), minor positive shifts of the tungstate-based redox potentials of PS-POM are observed. At $[TFA]/[PS-POM] = 1,000:1$, maximum shifts were approximately $+0.15$ V (Supplementary Fig. 19), which is in line with the literature^{24,39}. Based on the H^+/H_2 redox potential $E(H^+/H_2)$, in DMF which was reported as approximately -0.62 to -0.66 versus Fc^+/Fc ⁴⁰, it can be estimated that the one-electron reduced species is not reducing enough to drive the hydrogen evolution reaction efficiently the difference between two redox potentials ($\Delta E < 0.1$ V). By contrast, for the two-electron-reduced species, a redox potential difference of $\Delta E \approx 0.4$ V corresponds to a Gibbs free energy change of $\Delta G \approx -77$ kJ mol⁻¹, suggesting that the two-electron-reduced PS-POM is capable of spontaneous hydrogen evolution when reacted with a proton source.

At more negative potentials, cyclic voltammetry data show three Ru PS-based redox processes (assigned to $bpy/bpy^{\bullet-}$) at $E = -1.74$ V, -1.90 V and -2.15 V versus Fc^+/Fc (Supplementary Table 1 and Supplementary Fig. 16). This suggests that light-induced reductive quenching of the Ru PS (resulting in an electron stored on the bpy ligands) can generate a reduced species that can spontaneously transfer an electron to the POM (ΔG (first electron transfer) ≈ -102 kJ mol⁻¹, based on $\Delta E \approx 1.1$ V; ΔG (second electron transfer) ≈ -62 kJ mol⁻¹, based on $\Delta E \approx 0.6$ V). Due to the accessibility of two $W^{VI/V}$ redox couples, PS-POM is in principle capable of the light-driven storage of at least two electrons.

We then studied the spectro-electrochemistry of PS-POM under reductive conditions. This allowed us to correlate POM reduction with changes of the UV–vis/near-infrared (NIR) spectrum and thereby quantify the number of electrons stored on the POM (Supplementary Fig. 20). Spectro-electrochemistry shows that bulk electrolysis at potentials of -0.8 V and -1.1 V versus Fc^+/Fc results in the one- and two-electron reduction of the POM. For the one-electron reduced PS-POM, a characteristic broad $W^{VI/V}$ intervalence charge-transfer (IVCT) band at ~ 600 to 850 nm is observed, whereas for the two-electron-reduced PS-POM, a characteristic narrower IVCT band centred at ~ 650 nm is detected^{22,24}. Note that both one- and two-electron reduction result in the formation of stable, reduced PS-POM systems.

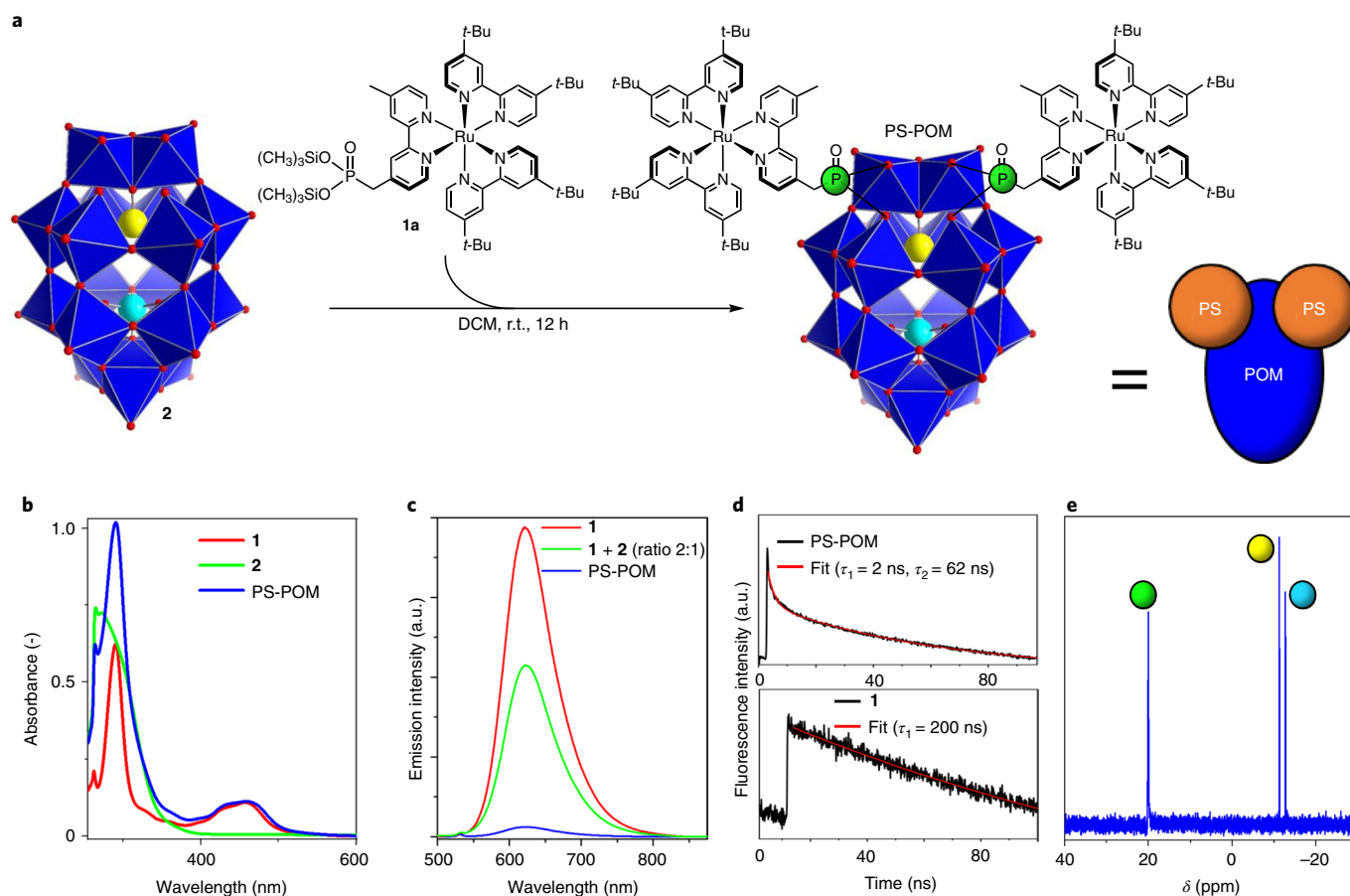


Fig. 2 | Synthesis and spectroscopic properties of PS-POM. **a**, Synthesis of PS-POM by reaction of the trimethylsilyl-phosphonate-functionalized Ru photosensitizer **1a** with the lacunary Dawson anion **2**, leading to the phosphonate-mediated covalent attachment of **1a** to **2**. Colour scheme: W, deep blue; O, red; P, green, yellow, light blue. r.t., room temperature; DCM, dichloromethane. **b**, UV-vis spectrum of PS-POM, **1** and **2**, showing that the PS absorption features are retained. **c**, Steady-state emission spectroscopy showing the emission quenching of PS-POM and the intermolecular references (**1** and **2**, 2:1 molar ratio). The high quenching efficiency in PS-POM indicates strong electronic coupling between the PS and POM components. Conditions: water-free, de-aerated DMF; PS-POM (3.2 μM); PS **1** (6.4 μM); POM **2** (3.2 μM). **d**, Emission decay profiles of PS-POM (top) and reference **1** (bottom), measured by time-correlated single-photon counting (in DMF; excitation wavelength $\lambda_{\text{excitation}} = 470$ nm). The data support strong electronic coupling between PS and POM, indicated by the steady-state emission spectroscopy shown in **c**. **e**, ^{31}P NMR spectrum of PS-POM in d_6 -DMSO (deuterated dimethyl sulfoxide) at room temperature; colour codes correspond to the phosphorus colour labels in **a**, indicating the presence of three distinct chemical environments for phosphorous in PS-POM.

Photochemical stability. Based on these findings, we hypothesized that efficient visible-light-driven electron transfer from PS to POM should be possible. To this end, we first explored the photochemical stability of PS-POM. Samples of PS-POM and the intermolecular reference (PS **1** and POM **2**, molar ratio 2:1) were dissolved in water-free de-aerated DMF and continuously irradiated with a monochromatic light-emitting diode (LED) light (maximum intensity wavelength $\lambda_{\text{max}} = 470$ nm, nominal power $P_{\text{nominal}} \approx 40 \text{ mW cm}^{-2}$) for 72 h. For PS-POM, only minimal changes of the PS-based absorbance were observed, while the non-linked PS **1** showed major PS degradation (absorbance loss at $\lambda = 462$ nm was $\sim 65\%$ after an irradiation time $t_{\text{irradiation}} = 72$ h; Fig. 3). We propose that this stability difference is based on the fast intramolecular electron transfer in PS-POM. This prevents the population of triplet metal-centered ^3MC excited states on the PS, which are known to trigger ligand dissociation⁴¹. These observations highlight the improved stability of the covalently linked PS-POM and forms the basis for its use as a photochemically robust molecular charge-separation and charge-storage system.

Ultrafast photophysics of PS-POM. Femtosecond pump-probe spectroscopy was used to analyse the excited-state relaxation in PS-POM, upon excitation of the $^1\text{MLCT}$ transition at 400 nm (Fig. 4; ref. 42). The initial signal is reminiscent of MLCT states in reference **1** and other $(\text{Ru}(\text{bpy})_3)^{2+}$ -based chromophores (Supplementary Fig. 22)^{43–45}. Within a few picoseconds, a pronounced excited-state absorption band appears at 500 nm. On a sub-hundred-picosecond timescale, this signal evolves into a long-lived species, with similar features as the long-lived $^3\text{MLCT}$ state in **1** and $(\text{Ru}(\text{bpy})_3)^{2+}$ -based systems (Fig. 4c and Supplementary Fig. 22). The data show that the spectral and kinetic responses of PS-POM are notably different from the typical properties of the pure PS **1** and the structurally similar prototype $(\text{Ru}(\text{bpy})_3)^{2+}$ (refs. 43–45). This indicates electronic coupling between the PS and POM in PS-POM, even on a sub-hundred-picosecond timescale. In other words, the coupling is already present in the electronically excited PS-POM dyad prior to the reductive quenching of the excited PS. Note that an in-depth analysis of the individual relaxation steps is outside the scope of this study.

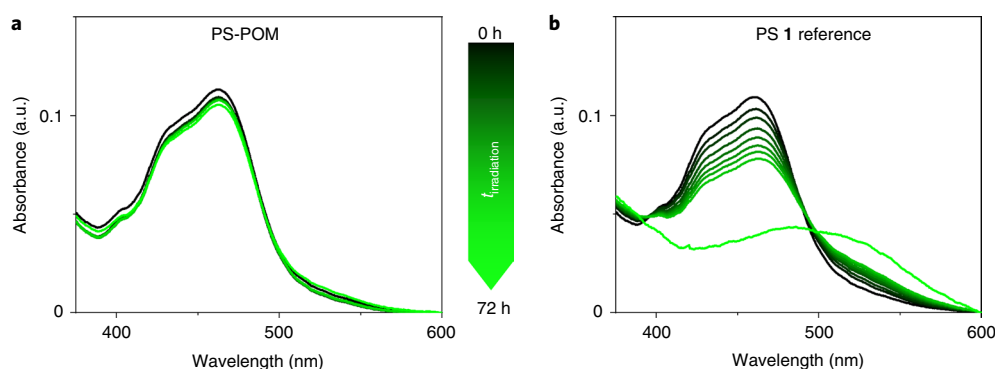


Fig. 3 | Irradiation stability assays for PS-POM and the POM-free PS reference system. **a**, UV-vis spectral changes of PS-POM (2.9 μM), showing that virtually no changes to the visible-light absorption are observed over the whole irradiation period (72 h). **b**, UV-vis spectral changes of the reference PS **1** (5.8 μM), showing major spectral changes under irradiation, indicative of (partial) PS degradation by ligand exchange. Conditions: solvent, DMF (water-free, de-aerated); irradiation using a monochromatic LED ($\lambda_{\text{max}} = 470 \text{ nm}$, $P_{\text{nominal}} \approx 40 \text{ mW cm}^{-2}$); $t_{\text{irradiation}} = 72 \text{ h}$.

Based on the available data, we interpret the processes underlying the data in Fig. 4a–c as follows: excitation of the $^1\text{MLCT}$ transition triggers a 3 ps process (inverse first-order rate constant τ_1), which leads to the appearance of a transient absorption feature between 500 and 550 nm. Based on UV-vis spectro-electrochemistry, this band is assigned to a reduced bpy ligand of the $\text{Ru}^{\text{III}}\text{-bpy}^{\text{+}}$ PS unit (Fig. 4c and Supplementary Figs. 22–24). This intermediate decays with a characteristic time constant of $\tau_2 = 12 \text{ ps}$, which is associated with an increased transient absorption signal above 600 nm. Both features are indicative of the formation of the reduced POM, that is, a charge-separated state $\text{PS}^{\text{+}}\text{-POM}^{\text{-}}$, where the characteristic broad red absorption of the POM is due to $\text{W}^{\text{VI/V}} \text{ IVCT}$ transitions⁴⁶ (see also UV-vis spectro-electrochemical data; Supplementary Figs. 20 and 24). The 90 ps component reflects the decay of the charge-separated state in the absence of a sacrificial electron donor. In addition, the transient absorption data show the presence of a second species whose spectrum is characteristic for a long-lived $^3\text{MLCT}$ state of the Ru PS. In sum, these results are consistent with the time-resolved emission studies (see above), which suggested the presence of two PS-POM ensembles. In one ensemble, emission is quenched rapidly due to PS-to-POM electron transfer. In the other ensemble, a long-lived, emissive $^3\text{MLCT}$ state is observed, which does not lead to PS-to-POM electron transfer. This difference could be associated with the presence of two PS-POM conformers due to the non-rigid, flexible linkage between PS and POM, resulting in different degrees of electronic coupling between PS and POM³².

PS-POM solutions for solar fuel storage. Next, we set out to demonstrate that light-driven charge separation, charge storage and fuel release is possible in the molecular PS-POM. To this end, we first targeted the light-driven reduction of PS-POM by irradiation into the PS MLCT band in the presence of a sacrificial electron donor such as sodium ascorbate (Asc), triethylamine (TEA) or triethanolamine (TEOA). As a reference example, water-free, de-aerated DMF solutions containing PS-POM (2.86 μM) and Asc (6.5 mM, 2,300 equiv.) were irradiated under argon with a monochromatic LED light source ($\lambda_{\text{max}} = 470 \text{ nm}$, $P_{\text{nominal}} \approx 40 \text{ mW cm}^{-2}$), and within a few seconds of irradiation, formation of the characteristic IVCT bands indicative of POM reduction were observed (Fig. 5). Quantitative UV-vis spectroscopic analysis shows that after 6 min of irradiation, the system reaches an equilibrated state where we observe an average reduction of PS-POM by approximately two electrons (Fig. 5 and Supplementary Figs. 11 and 12). Note that without irradiation, no light-independent reaction between PS-POM and the respective electron donor was observed. Photoreduction of PS-POM using the

sacrificial electron donor Asc was notably faster compared with the sacrificial donor TEOA (Supplementary Fig. 12). We suggest this is due to a more efficient photochemical mechanism in the case of Asc (quantum efficiency $\Phi = 0.25\%$) compared with TEOA (quantum efficiency $\Phi = 0.05\%$).

In-situ resonance Raman spectro-electrochemistry was used to verify the stability of the reduced PS-POM species. The study used stepwise electrochemical reduction of PS-POM to mimic the stepwise photoreduction of PS-POM (Supplementary Fig. 25). The data obtained is in line with in-situ UV-vis/NIR spectroscopy (Fig. 5 and Supplementary Figs. 11 and 12) and shows that stepwise reduction of the POM subunit does not affect the stability and chromophoric properties of PS-POM.

In the absence of oxygen, the reduced PS-POM solution is chemically stable and can be stored in the dark for prolonged periods. A slow reoxidation of the solution is observed, resulting in a half-life of the reduced PS-POM of $t_{1/2} > 24 \text{ h}$ (Supplementary Fig. 15). The background reoxidation is assigned to a hydrogen evolution reaction due to the presence of protons in solution (for example, from the sacrificial electron donors) as well as other reoxidation pathways that are still under investigation. By contrast, under identical reaction conditions, notably shorter half-lives of the reduced states were observed for the non-covalently linked reference systems PS **1** and POM **2** ($t_{1/2} \approx 5 \text{ min}$) and PS **1** and Bz-POM ($t_{1/2} \approx 14 \text{ min}$; Supplementary Fig. 15, Bz-POM: bis-benzylphosphonate-functionalized **2**, $(n\text{Bu}_4\text{N})_3\text{K}(\alpha_2\text{-P}_2\text{W}_{17}\text{O}_{61}(\text{POCH}_2\text{C}_6\text{H}_5))$; details in Supplementary Section 2. We attribute this discrepancy to the different electronic structure and charge stabilization/delocalization in PS-POM, which results in improved electron storage times.

Delayed on-demand H_2 production. Next, we explored the on-demand hydrogen evolution from photochemically reduced PS-POM solutions. To this end, water-free, de-aerated DMF solutions containing PS-POM (9 μM) and sacrificial electron donor (Asc, 6.5 mM, 720 equiv.) were irradiated under argon for 15 min using a monochromatic LED light source ($\lambda_{\text{max}} = 470 \text{ nm}$, $P_{\text{nominal}} \approx 40 \text{ mW cm}^{-2}$) in a closed vessel equipped with a septum. This led to the formation of the two-electron-reduced PS-POM as shown by UV-vis spectroscopy (Fig. 5 and Supplementary Fig. 12). The addition of a proton donor (H_2SO_4 , 4.0 M in DMF, 500 μl) led to the instantaneous evolution of H_2 as identified and quantified by headspace gas chromatography. Under the given conditions, we observed an H_2 formation yield of $\sim 40\%$ of the theoretical value (based on the ratio of electrons stored on PS-POM and evolved H_2 ; details in Supplementary Table 2). To simulate storage

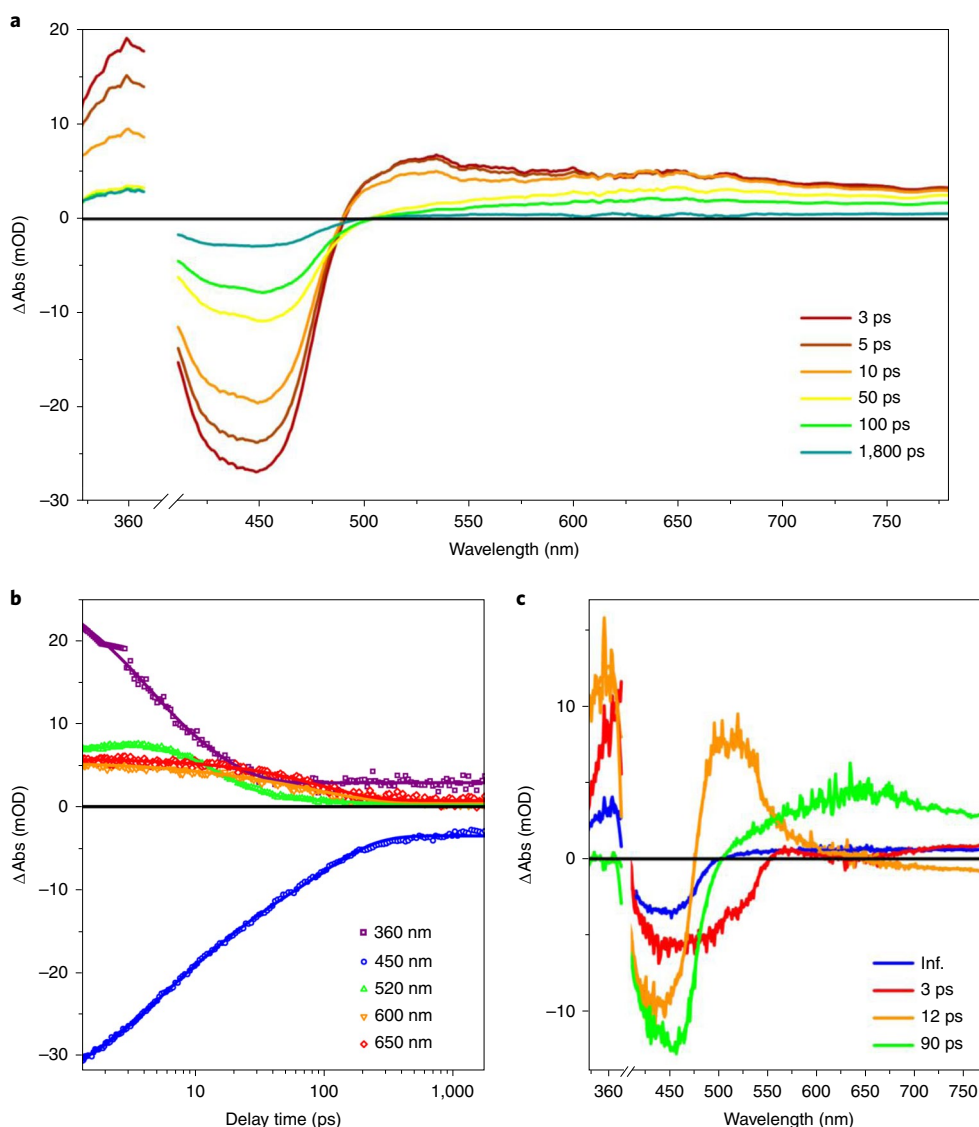


Fig. 4 | Photophysical properties of PS-POM. **a**, Transient absorption spectra at selected delay times. **b**, Transient kinetics at key wavelengths. **c**, Spectral changes associated with each kinetic process (decay-associated spectra) for PS-POM (0.3 mM in DMF), pumped at 400 nm. Upon excitation of the MLCT transitions in the PS unit, a $\text{Ru}^{\text{III}}\text{-bpy}^{\text{+}}$ species is formed within 3 ps (τ_1), which shows distinct spectral features of the reduced $\text{bpy}^{\text{+}}$ ligand (also Supplementary Fig. 27). The transient absorption spectrum at 12 ps (τ_2) displays a broad absorption band above 600 nm, due to the characteristic IVCT absorption of the reduced POM in the charge-separated state. Subsequently, the charge-separated state decays to the ground state with a characteristic time constant of 90 ps (τ_3). ΔAbs , change in absorbance; Inf., infinite component.

and on-demand hydrogen release, we performed the reduction/hydrogen-release experiment described above; however, we stored the reduced PS-POM solution for 2.5 h under an inert atmosphere before the acid-induced hydrogen release. Here, we observed that the H_2 formation yield dropped from 40% to 33% of theory. This shows that ‘dark’ background reactions are present that need to be identified for system optimization. UV-vis spectroscopy shows that in these experiments, PS-POM is fully discharged; that is, the POM subunit is fully reoxidized to an all-W(VI) state. This highlights that other, thus far unknown side reactions are expected to cause the deviation between the calculated and observed H_2 yield. Identification of these reactions as a basis for the selectivity-tuning of the reaction system is a key target for future studies.

To gain insight into the kinetics of hydrogen evolution, we used time-resolved UV-vis spectroscopy to assess temporal changes of the local maximum at $\lambda = 650$ nm (that is, the IVCT band indicative

of reduced PS-POM) upon addition of the proton source sulfuric acid under inert, oxygen-free conditions in a glove box. As shown in Figs. 5 and 6, we note a complete disappearance of the IVCT band within <10 s, highlighting the fast kinetics of H_2 formation (as verified by gas chromatography). Note that the reduced PS-POM can also be reoxidized by atmospheric oxygen; however, this process shows markedly different kinetics (Supplementary Fig. 26).

Conclusions

This study reports a purely molecular photochemical device capable of decoupling light and dark reactions in solar hydrogen production. The molecular PS-POM dyad shows excellent chemical and photochemical stability. Under visible-light irradiation, PS-POM is reduced and can store two electrons per dyad molecule. The stable reduced PS-POM system can be stored under dark conditions in the absence of oxygen. Hydrogen on-demand experiments

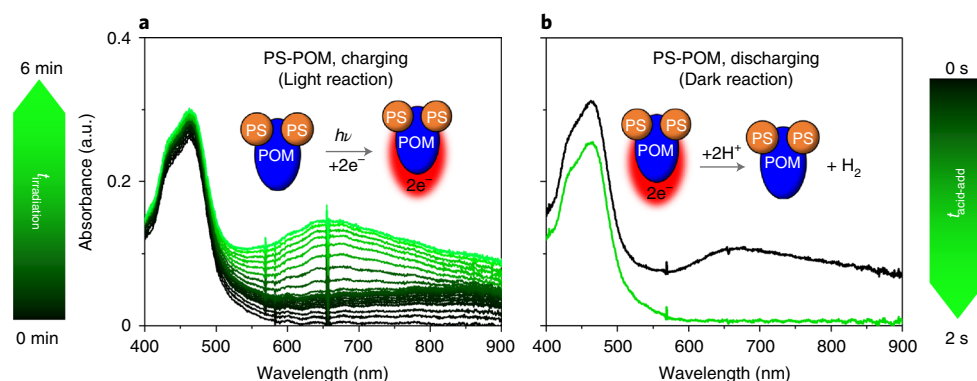


Fig. 5 | Spectral evolution of PS-POM upon photoreduction and acid addition. **a**, UV-vis spectral changes of PS-POM (9 μM) upon irradiation using a monochromatic LED ($\lambda_{\text{max}} = 470 \text{ nm}$, $P_{\text{nominal}} \approx 40 \text{ mW cm}^{-2}$) in the presence of a sacrificial electron donor (TEOA, 60 mM, 6,700 equiv.); the data show that under the given conditions, electron transfer and storage on the POM unit is possible, indicated by the characteristic, broad IVCT absorption band centred at 650 nm. **b**, Normalized UV-vis spectral changes of PS-POM (9 μM) upon addition of a proton source (H_2SO_4 , 100 mM, 11,000 equiv.), showing the virtually instantaneous electron release by reaction of PS-POM with protons, resulting in H_2 formation (confirmed by gas chromatography). h , Planck constant; ν , light frequency; $h\nu$, light energy / irradiation, i.e., that this reaction is light-driven; $t_{\text{acid-add}}$, time after acid-addition.

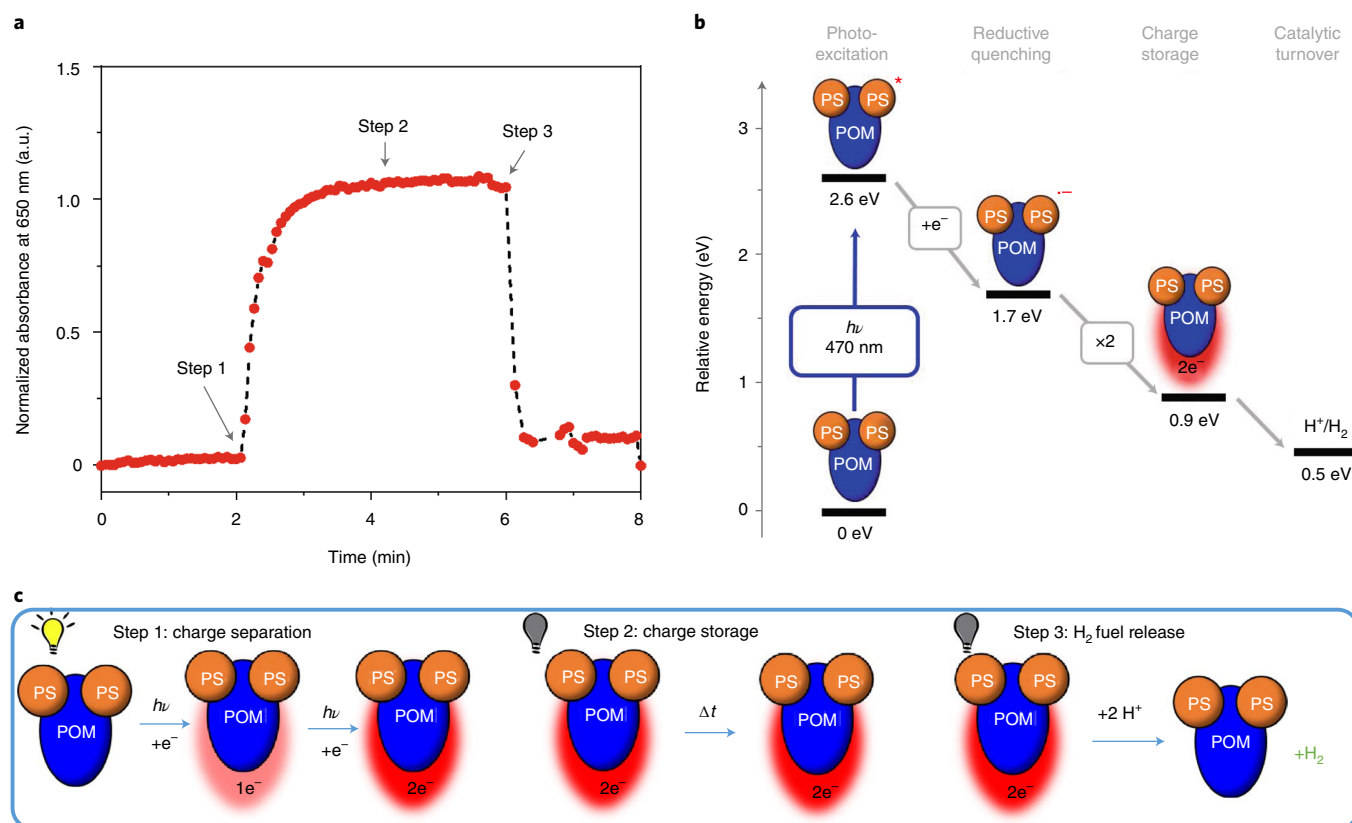


Fig. 6 | Delayed on-demand hydrogen production. **a**, Time-dependent UV-vis spectroscopic analysis of the absorption maximum at 650 nm during charging (Step 1, beginning at arrow), storage (Step 2) and discharging (Step 3, beginning at arrow), highlighting the light-induced accumulation of electrons on the POM unit as well as their release by reaction with a proton source. Conditions: solvent, water-free, de-aerated DMF; irradiation using a monochromatic LED ($\lambda_{\text{max}} = 470 \text{ nm}$, $P_{\text{nominal}} \approx 40 \text{ mW cm}^{-2}$); proton donor, H_2SO_4 in DMF (4.0 M); [PS-POM] = 9 μM ; sacrificial electron donor, TEOA (60 mM, 6,700 equiv.). TEOA was chosen to facilitate observation of the reduction process due to the slower PS-POM/TEOA reduction kinetics compared with other electron donors. **b**, Simplified energy scheme showing the energies and transitions between different experimentally observed intermediates of the on-demand hydrogen production experiment (Supplementary Section 7 for details) * marks the photoexcited system. **c**, Schematic illustration of the stepwise charging (Step 1), storage (Step 2) and discharging (Step 3) of the PS-POM solution, summarizing the light-dependent and light-independent reactions studied for PS-POM. Δt , delay time.

showed that reaction of the reduced PS-POM with a proton source results in instant hydrogen evolution (current H_2 yield, 40%), while PS-POM is fully reoxidized. This study therefore reports a single

molecule dyad capable of light absorption, charge separation/storage and fuel release in which light and dark reactions can be spatially and temporally decoupled. It can serve as a blueprint for

molecular architectures for scalable, decentralized liquid energy storage systems.

Online content

Any methods, additional references, Nature Research reporting summaries, source data, extended data, supplementary information, acknowledgements, peer review information; details of author contributions and competing interests; and statements of data and code availability are available at <https://doi.org/10.1038/s41557-021-00850-8>.

Received: 26 November 2020; Accepted: 26 October 2021;

Published online: 27 January 2022

References

- Roger, I., Shipman, M. A. & Symes, M. D. Earth-abundant catalysts for electrochemical and photoelectrochemical water splitting. *Nat. Rev. Chem.* **1**, 0003 (2017).
- Chen, S., Takata, T. & Domen, K. Particulate photocatalysts for overall water splitting. *Nat. Rev. Mater.* **2**, 17050 (2017).
- Listorti, A., Durrant, J. & Barber, J. Artificial photosynthesis: solar to fuel. *Nat. Mater.* **8**, 929–930 (2009).
- Cook, T. R. et al. Solar energy supply and storage for the legacy and nonlegacy worlds. *Chem. Rev.* **110**, 6474–6502 (2010).
- Rausch, B., Symes, M. D., Chisholm, G. & Cronin, L. Decoupled catalytic hydrogen evolution from a molecular metal oxide redox mediator in water splitting. *Science* **345**, 1326–1330 (2014).
- Symes, M. D. & Cronin, L. Decoupling hydrogen and oxygen evolution during electrolytic water splitting using an electron-coupled-proton buffer. *Nat. Chem.* **5**, 403–409 (2013).
- Borgschulte, A. The hydrogen grand challenge. *Front. Energy Res.* **4**, 11 (2016).
- McHugh, P. J., Stergiou, A. D. & Symes, M. D. Decoupled electrochemical water splitting: from fundamentals to applications. *Adv. Energy Mater.* **10**, 2002453 (2020).
- Huang, J. & Wang, Y. Efficient renewable-to-hydrogen conversion via decoupled electrochemical water splitting. *Cell Rep. Phys. Sci.* **1**, 100138 (2020).
- Ifkovits, Z. P., Evans, J. M., Meier, M. C., Papadantonakis, K. M. & Lewis, N. S. Decoupled electrochemical water-splitting systems: a review and perspective. *Energy Environ. Sci.* <https://doi.org/10.1039/D1EE01226F> (2021).
- Yan, Z., Hitt, J. L., Turner, J. A. & Mallouk, T. E. Renewable electricity storage using electrolysis. *Proc. Natl Acad. Sci. USA* **117**, 12558–12563 (2020).
- Pellow, M. A., Emmott, C. J. M., Barnhart, C. J. & Benson, S. M. Hydrogen or batteries for grid storage? A net energy analysis. *Energy Environ. Sci.* **8**, 1938–1952 (2015).
- Rothschild, A. & Dotan, H. Beating the efficiency of photovoltaics-powered electrolysis with tandem cell photoelectrolysis. *ACS Energy Lett.* **2**, 45–51 (2017).
- Sakar, M., Nguyen, C.-C., Vu, M.-H. & Do, T.-O. Materials and mechanisms of photo-assisted chemical reactions under light and dark conditions: can day–night photocatalysis be achieved? *ChemSusChem* **11**, 809–820 (2018).
- Bloor, L. G. et al. Solar-driven water oxidation and decoupled hydrogen production mediated by an electron-coupled-proton buffer. *J. Am. Chem. Soc.* **138**, 6707–6710 (2016).
- Lau, V. W. et al. Dark photocatalysis: storage of solar energy in carbon nitride for time-delayed hydrogen generation. *Angew. Chem. Int. Ed.* **129**, 525–529 (2017).
- Konduri, R. et al. Ruthenium photocatalysis capable of reversibility storing up to four electrons in a single acceptor ligand: a step closer to artificial photosynthesis. *Angew. Chem. Int. Ed.* **41**, 3185–3187 (2002).
- Schulz, M. et al. Photoinduced charge accumulation and prolonged multielectron storage for the separation of light and dark reaction. *J. Am. Chem. Soc.* **142**, 15722–15728 (2020).
- Proust, A. et al. Functionalization and post-functionalization: a step towards polyoxometalate-based materials. *Chem. Soc. Rev.* **41**, 7605–7622 (2012).
- Anyushin, A. V., Kondinski, A. & Parac-Vogt, T. N. Hybrid polyoxometalates as post-functionalization platforms: from fundamentals to emerging applications. *Chem. Soc. Rev.* **49**, 382–432 (2020).
- Matt, B. et al. Elegant approach to the synthesis of a unique heteroleptic cyclometalated iridium(III)-polyoxometalate conjugate. *Organometallics* **31**, 35–38 (2012).
- Matt, B. et al. Long lived charge separation in iridium(III)-photosensitized polyoxometalates: synthesis, photophysical and computational studies of organometallic-redox tunable oxide assemblies. *Chem. Sci.* **4**, 1737–1745 (2013).
- Parrot, A. et al. Photochromism and dual-color fluorescence in a polyoxometalate-benzospiropyran molecular switch. *Angew. Chem. Int. Ed.* **56**, 4872–4876 (2017).
- Matt, B. et al. Charge photo-accumulation and photocatalytic hydrogen evolution under visible light at an iridium(III)-photosensitized polyoxotungstate. *Energy Environ. Sci.* **6**, 1504–1508 (2013).
- Schönweiz, S. et al. Experimental and theoretical investigation of the light-driven hydrogen evolution by polyoxometalate–photosensitizer dyads. *Chem. Eur. J.* **23**, 15370–15376 (2017).
- Luo, Y. et al. Yield—not only lifetime—of the photoinduced charge-separated state in iridium complex–polyoxometalate dyads impact their hydrogen evolution reactivity. *Chem. Eur. J.* **26**, 8045–8052 (2020).
- Luo, Y. et al. Is electron ping-pong limiting the catalytic hydrogen evolution activity in covalent photosensitizer–polyoxometalate dyads? *Chem. Commun.* **56**, 10485–10488 (2020).
- Schaming, D. et al. Synthesis and photocatalytic properties of mixed polyoxometalate–porphyrin copolymers obtained from Anderson-type polyoxomolybdates. *Langmuir* **26**, 5101–5109 (2010).
- Schönweiz, S. et al. Covalent photosensitizer–polyoxometalate–catalyst dyads for visible-light-driven hydrogen evolution. *Chem. Eur. J.* **22**, 12002–12005 (2016).
- Azcarate, I. et al. Generation of photocurrent by visible-light irradiation of conjugated Dawson polyoxophosphovanadotungstate–porphyrin copolymers. *Chem. Eur. J.* **21**, 8271–8280 (2015).
- Black, F. A. et al. Rapid photoinduced charge injection into covalent polyoxometalate–bodipy conjugates. *Chem. Sci.* **9**, 5578–5584 (2018).
- Odobel, F. et al. Coupled sensitizer–catalyst dyads: electron-transfer reactions in a perylene–polyoxometalate conjugate. *Chem. Eur. J.* **15**, 3130–3138 (2009).
- Toupalas, G. et al. Tuning photoinduced electron transfer in POM–bodipy hybrids by controlling the environment: experiment and theory. *Angew. Chem. Int. Ed.* **60**, 6518–6525 (2021).
- Kirchhoff, B., Rau, S. & Streb, C. Detecting and preventing the formation of photosensitizer–catalyst colloids in homogeneous light-driven water oxidation. *Eur. J. Inorg. Chem.* **2016**, 1425–1429 (2016).
- Heussner, K., Peuntinger, K., Rockstroh, N., Rau, S. & Streb, C. Cluster-controlled dimerisation in supramolecular ruthenium photosensitizer–polyoxometalate systems. *Dalton Trans.* **44**, 330–337 (2015).
- Heussner, K. et al. Solution and solid-state interactions in a supramolecular ruthenium photosensitizer–polyoxometalate aggregate. *Chem. Commun.* **47**, 6852–6854 (2011).
- Amthor, S. et al. Tailored protective groups for surface immobilization of ruthenium dyes. *Dalton Trans.* **49**, 3735–3742 (2020).
- Streb, C. New trends in polyoxometalate photoredox chemistry: from photosensitisation to water oxidation catalysis. *Dalton Trans.* **41**, 1651–1659 (2012).
- Prenzler, P. D., Boskovic, C., Bond, A. M. & Wedd, A. G. Coupled electron- and proton-transfer processes in the reduction of α -[P₂W₁₈O₆₂]⁶⁻ and α -[H₂W₁₂O₄₀]⁶⁻ as revealed by simulation of cyclic voltammograms. *Anal. Chem.* **71**, 3650–3656 (1999).
- Pegis, M. L. et al. Standard reduction potentials for oxygen and carbon dioxide couples in acetonitrile and N,N-dimethylformamide. *Inorg. Chem.* **54**, 11883–11888 (2015).
- Soupart, A., Alary, F., Heully, J. L., Elliott, P. I. P. & Dixon, I. M. Recent progress in ligand photorelease reaction mechanisms: theoretical insights focusing on Ru(II) ³MC states. *Coord. Chem. Rev.* **408**, 213184 (2020).
- Siebert, R. et al. Spectroscopic investigation of the ultrafast photoinduced dynamics in π -conjugated terpyridines. *ChemPhysChem* **10**, 910–919 (2009).
- Damrauer, N. H. Femtosecond dynamics of excited-state evolution in [Ru(bpy)₃]²⁺. *Science* **275**, 54–57 (1997).
- Tarnovsky, A. N., Gawelda, W., Johnson, M., Bressler, C. & Chergui, M. Photocyclization of aqueous ruthenium(II)-tris-(2,2'-bipyridine) with high-intensity femtosecond laser pulses. *J. Phys. Chem. B* **110**, 26497–26505 (2006).
- Müller, P. & Brettel, K. [Ru(bpy)₃]²⁺ as a reference in transient absorption spectroscopy: differential absorption coefficients for formation of the long-lived ³MLCT excited state. *Photochem. Photobiol. Sci.* **11**, 632–636 (2012).
- Kemmegne-Mbouguen, J. C. et al. Electrochemical properties of the [SiW₁₀O₃₆(M₂O₂E₂)]⁶⁻ polyoxometalate series (M = Mo(V) or W(V); E = S or O). *New J. Chem.* **43**, 1146–1155 (2019).

Publisher's note Springer Nature remains neutral with regard to jurisdictional claims in published maps and institutional affiliations.

© The Author(s), under exclusive licence to Springer Nature Limited 2022

Methods

Synthesis and characterization of PS-POM. 1 (0.285 g, 0.23 mmol, 2.8 equiv.; Supplementary Section 2) was dissolved in de-aerated DCM (10 ml) in a glove box, and trimethylsilyl bromide (TMSBr; 130 μ l, 0.91 mmol, 4 equiv.) was added to the solution, resulting in the formation of **1a**, that is, TMS-functionalized **1** (Fig. 2a). The mixture was stirred for 12 h at room temperature. Then, the solvent and excess TMSBr were removed under reduced pressure. The residue was taken up in a small amount of DCM (~5 ml) and filtered through a frit (porosity 4). The obtained solution was diluted to a volume of 10 ml with DCM and stirred for 5 min at room temperature. (*n*-Bu₄N)₇K₃(α -P₂W₁₇O₆₁) (0.480 g, 0.08 mmol, 1 equiv.; Supplementary Section 2) was added as a solid to the solution. Upon addition, the solution decolourized immediately. The suspension was further stirred for 12 h at room temperature. After that time, the solid was filtered off and washed with DCM until the filtrate was clear. The crude product was purified by slow diffusion of DCM into a DMF solution (50 ml), giving an orange-red powder. The powder was recovered by centrifugation and washed with DCM, then dissolved in 5 ml DMF. To the solution, 1.5 g *n*-Bu₄NCl (5.4 mmol) were added. To this, water (25 ml) was added, resulting in an orange precipitate. The precipitate was washed with a water/ethanol solution (30 ml:5 ml), ethanol (2 \times 25 ml) and diethyl ether (2 \times 25 ml). The precipitate was redissolved in DMF (50 ml). Slow diffusion of DCM into this solution gave an orange-red powder, which was recovered by filtration, washed with diethyl ether and dried to give the pure PS-POM, (*n*-Bu₄N)K(P₂W₁₇O₆₁((mPO₃)₂bpy)Ru(tbbpy)₂). The yield was 280 mg (0.045 mmol), 57% based on (*n*-Bu₄N)₇K₃(α -P₂W₁₇O₆₁). The ¹H NMR (400 MHz, DMSO) was as follows (δ in ppm): δ 8.77 (*dd*, *J* = 16.7, 14.0 Hz, ¹⁰H), 8.47 (*d*, *J* = 4.5 Hz, ²H), 7.71–7.47 (*m*, ²²H), 7.40 (*dd*, *J* = 10.3, 4.4 Hz, ²H), 1.51–1.62 (*m*, ⁶H) and 1.44–1.34 (*m*, ⁷²H); the ³¹P NMR (162 MHz, DMSO) was (δ in ppm): δ 20.14, 20.01, –11.26 and –12.70. For the matrix-assisted laser desorption/ionization–time of flight (Peptide Mix, negative-ion mode), the mass to charge ratio *m/z* calculated for C₁₁₂H₁₅₆N₁₃O₆₁P₂Ru₂ was 3,080; *m/z* observed was 3,080 (M – (K⁺) – (*n*Bu₄N⁺) + (H₂O)²⁻, where M = the complete PS-CAT molecule including its cations.

Photostability studies. Photostability experiments were conducted in water-free, de-aerated DMF at the following concentrations: [PS-POM] = 2.9 μ M and [**1**] = 5.8 μ M. The samples were irradiated using a 470 nm LED with power *P* \approx 40–50 mW cm^{–2}, integrated into a custom reactor cooled by four fans, to control room temperature during irradiation.

Photochemical reduction experiments. Photochemical reduction studies were carried out in water-free, de-aerated DMF solution at the following concentrations: [**1**] = 5.8 μ M, [**2**] = 2.9 μ M and [PS-POM] = 2.9 μ M, unless stated otherwise. The stock solutions were prepared under air, degassed with argon (1 min ml^{–1}) and kept in an argon-filled glove box. Stock solution aliquots were transferred into gas-tight quartz glass cuvettes (optical path length *d* = 10.0 mm). The samples were irradiated using 470 nm LEDs (*P* \approx 40–50 mW cm^{–2}) integrated in a custom-built reactor cooled by four fans, to maintain room temperature during irradiation.

Hydrogen evolution experiments. Hydrogen evolution experiments were conducted using Schlenk tubes (borosilicate glass, volume of ~21 ml) sealed by a rubber septum, which was exchanged after every measurement. For a standard experiment, PS-POM and sacrificial electron donor were dissolved under an argon atmosphere in water-free, de-aerated DMF at the concentrations given in the manuscript. The PS-POM solution was irradiated (monochromatic LED; λ_{max} , 470 nm) for the desired period of time. The PS-POM reduction state was monitored by UV-vis/NIR spectroscopy as described in the manuscript. Hydrogen release is possible by addition of the proton donor sulfuric acid to the reaction vessel via a Hamilton syringe (500 μ l, 4 M in DMF), and the mixture was allowed to react for 5 min in the dark. Subsequent headspace gas chromatography was used to quantify H₂ evolution. Exclusion experiments confirmed that no hydrogen is formed in the absence of PS-POM, light or sacrificial electron donor. No hydrogen was detected when PS **1** was irradiated in the presence of an electron donor.

Gas chromatography. Gas chromatography was performed on a Bruker Scion gas chromatography mass spectrometry instrument with a thermal conductivity detector (column specifications: molecular sieve, 5 Å; column length *l* = 75 m; column diameter *d* = 0.53 mm; oven temperature, 70 °C; flow rate, 30 ml min^{–1}; detector temperature, 200 °C) with argon as the carrier gas. The gas chromatography was calibrated by direct injection of known amounts of H₂ gas.

Resonance Raman spectroscopy and spectro-electrochemistry. For resonance Raman spectroscopy, visible diode lasers at 405 nm (TopMode-405-HP, Toptica), 473 nm (HB-Laser), 532 nm (HB-Laser) and 643 nm (CrystaLaser) were used for excitation. For spectral detection, an IsoPlane 160 spectrometer (Princeton Instruments) was used, applying an entrance slit width of 50 μ m and diffraction gratings with either 2,400 or 1,200 grooves per millimetre. The laser power was attenuated to approximately 5 mW to reduce photodegradation of the analyte. The Raman-scattered signals were collected in transmission and filtered from laser light using dielectric long-pass filters (Semrock) before being focused

onto the spectrograph's entrance slit. The spectrally dispersed, Raman-scattered photons were detected by a thermoelectrically cooled charge-coupled device camera of 1,340 \times 100 pixels (PIXIS eXcelon, Princeton Instruments). The band of DMF at 1,407 cm^{–1} was used as a reference for normalizing Raman intensities and calibration of the wave number scale. Spectral postprocessing includes background correction, normalization and subtraction of the solvent spectrum. Spectro-electrochemical measurements were performed in a fused silica cuvette of 1 mm path length (Hellma, Bioanalytical Systems) employing a three-electrode configuration consisting of a Pt counter electrode, an Ag/AgCl pseudo-reference electrode and a glassy carbon working electrode. Potential-controlled monitoring of spectral changes as well as cyclic voltammetry were carried out using a computer-controlled VersaSTAT 3 potentiostat (Princeton Applied Research).

Transient absorption spectroscopy. Femtosecond transient absorption data were recorded using a custom-built optical set-up reported earlier⁴². For excitation, a 1-kHz-pulse repetition rate Ti-sapphire regenerative amplifier (Libra, Coherent) was used. A fraction of the laser output is focused into a CaF₂ plate mounted on a rotating stage for generating the white-light supercontinuum pulse. This broad band pulse is split in the reference and probe pulse. The other part of the laser output is used to generate the pump pulse of roughly 100 fs pulse duration by second harmonic generation (SHG) of the fundamental in a nonlinear crystal (400 nm). A mechanical chopper is used to reduce the repetition rate of the pump pulses to 0.5 kHz, and the mutual polarization of the pump and probe pulses is adjusted to the magic angle of 54.7° by a Berek compensator and a polarizer. The probe pulse is focused into the 1 mm cuvette using a 500-mm-focal-length concave mirror. The spectra of probe and reference pulses are detected by a Czerny–Turner spectrograph of 150 mm focal length (SP2150, Princeton Instruments) equipped with a diode array detector (Pascher Instruments). During ~300 fs around time zero, strong contributions from coherent artefact signals⁴⁷ are observed, which inhibit analysing the pump–probe data by multi-exponential fitting algorithms at a shorter time delay. Data analysis includes first a spectral preprocessing step for chirp correction before a sum of exponential functions is fitted to the data by least squares regression analysis using custom software (Pascher Instruments). The pulse overlap region of \pm 150 fs is removed from the data analysis due to the coherent artefacts mentioned above. The amplitudes of the exponential fit correspond to the decay-associated spectra. For the investigation of the primary photoinduced processes, the sample was dissolved in anhydrous DMF (optical density at a wavelength of 400 nm OD (400 nm) = 0.3 in a cell with 1 mm path length).

Nanosecond transient emission spectroscopy. Nanosecond transient emission spectroscopy was used to study the lifetime of the long-lived species. The pump pulses centred at 355 nm were produced by a Continuum Surelite Nd:Y₃Al₅O₁₂ (Nd:YAG) laser system (pulse duration, 5 ns; repetition rate, 10 Hz). A Continuum OPO Plus pumped by a Continuum Surelite Nd:YAG laser generated the pump pulses at 470 nm. The power of the pump beam was kept at 0.2 mJ per pulse. The probe light was provided by a 75 W xenon arc lamp. Spherical concave mirrors were used to focus the probe beam into the samples and then to send the beam to the monochromator (Acton, Princeton Instruments). The spectrally selected probe light was detected by a Hamamatsu R928 photomultiplier. Time-resolved emission spectra were recorded by using a 475 nm long-pass filter before the detector to eliminate the pump scattering. The signal was amplified and processed by a commercially available detection system (Pascher Instruments). Each sample was freshly prepared, and its optical density was kept at ~0.2 at the excitation wavelength. All measurements were performed in 1-cm-path-length fluorescence cuvettes. The stability of the samples during all spectroscopic experiments was checked by measuring absorption spectra before and after each spectroscopic run.

Spectro-electrochemical characterization. Time-dependent UV-vis absorption spectra were recorded with an Avantes AvaSpec-ULS2048CL-EVO-(CMOS) spectrophotometer connected to an Avantes AvaLight-DH-S-BAL light source via fibre-optic cables. The data acquisition time was 1.5 ms and averaged over 100 measurements. UV-vis spectro-electrochemical measurements at room temperature were conducted with a commercial honeycomb thin-layer spectro-electrochemistry cell (Pine Research Instrumentation), employing a screen-printed platinum working electrode and counter electrode and a Ag/Ag⁺ (0.01 M AgNO₃ in acetonitrile) reference electrode. The effective path length was 1.7 mm. Constant cell potentials were applied during the spectro-electrochemistry measurements using an Autolab potentiostat PGSTAT204 (Metrohm).

Data availability

All the data supporting the findings of this study are available within the main text of the paper and the Supplementary Information and have been deposited on Zenodo.org under <https://doi.org/10.5281/zenodo.5533869>. Crystallographic data for the structure reported in this Article has been deposited at the Cambridge Crystallographic Data Centre, under deposition number CCDC no. 2045447. Copies of the data can be obtained free of charge via <https://www.ccdc.cam.ac.uk/structures/>.

References

47. Dobryakov, A. L., Kovalenko, S. A. & Ernsting, N. P. Coherent and sequential contributions to femtosecond transient absorption spectra of a rhodamine dye in solution. *J. Chem. Phys.* **123**, 044502 (2005).

Acknowledgements

We gratefully acknowledge the Deutsche Forschungsgemeinschaft DFG for financial support through the TRR234 'CataLight' (project no. 364549901, projects A1, A4, B2, B6 and Z2; U.S.S., S.R., B.D. and C.S.). Funding by the Federal State of Baden-Württemberg and Ulm University for a PhD fellowship (LGFG; S.K.) and a Margarete von Wrangell fellowship (M.A.) is gratefully acknowledged. We thank T. Meyer-Zedler for assistance with the time-resolved emission measurements.

Author contributions

S.A., S.K., A.K.M., S.R., B.D. and C.S. conceived the experiments and performed data analyses. S.A. and S.K. performed syntheses and characterization. S.A. and M.H. performed catalytic tests. C.L., L.Z. and B.D. performed time-resolved spectroscopy

and provided data interpretation. D.N. and M.A. performed electrochemistry. W.T. and U.S.S. provided mass-spectrometric data. A.K.M. performed crystallography. All authors cowrote the manuscript.

Competing interests

The authors declare no competing interests.

Additional information

Supplementary information The online version contains supplementary material available at <https://doi.org/10.1038/s41557-021-00850-8>.

Correspondence and requests for materials should be addressed to Benjamin Dietzek-Ivanšić, Sven Rau or Carsten Streb.

Peer review information *Nature Chemistry* thanks the anonymous reviewers for their contribution to the peer review of this work.

Reprints and permissions information is available at www.nature.com/reprints.